INTERNATIONAL JOURNAL FOR NUMERICAL METHODS IN FLUIDS
Int. J. Numer. Meth. Fluids 2005; **49**:739–761

Time-dependent turbulent cavitating flow computations with interfacial transport and filter-based models

Jiongyang Wu[1,‡], Guoyu Wang[2,§] and Wei Shyy[3,*,†]

[1] *Department of Mechanical and Aerospace Engineering, University of Florida, P.O. Box 116250, 231 MAE-A BLD, Gainesville, FL 32611, U.S.A.*
[2] *School of Vehicle and Transportation Engineering, Beijing Institute of Technology, No. 5 Zhongguancun Nandajie Haidian District, Beijing 10081, People's Republic of China*
[3] *Department of Aerospace Engineering, University of Michigan, 3064 FXB, 1320 Beal Avenue, Ann Arbor, MI 48109-2140, U.S.A.*

SUMMARY

Turbulent cavitating flow computations need to address both cavitation and turbulence modelling issues. A recently developed interfacial dynamics-based cavitation model (IDCM) incorporates the interfacial transport into the computational modelling of cavitation dynamics. For time-dependent flows, it is known that the engineering turbulence closure such as the original k–ε model often over-predicts the eddy viscosity values reducing the unsteadiness. A recently proposed filter-based modification has shown that it can effectively modulate the eddy viscosity, rendering better simulation capabilities for time-dependent flow computations in term of the unsteady characteristics. In the present study, the IDCM along with the filter-based k–ε turbulence model is adopted to simulate 2-D cavitating flows over the Clark-Y airfoil. The chord Reynolds number is $Re = 7.0 \times 10^5$. Two angles-of-attack of 5 and 8° associated with several cavitation numbers covering different flow regimes are conducted. The simulation results are assessed with the experimental data including lift, drag and velocity profiles. The interplay between cavitation and turbulence models reveals substantial differences in time-dependent flow results even though the time-averaged characteristics are similar. Copyright © 2005 John Wiley & Sons, Ltd.

KEY WORDS: cavitation; turbulence; time-dependent; filter-based; interfacial

---

[*] Correspondence to: Wei Shyy, Department of Aerospace Engineering, University of Michigan, 3064 FXB, 1320 Beal Avenue, Ann Arbor, MI 48109-2140, U.S.A.
[†] E-mail: weishyy@umich.edu
[‡] E-mail: wujy@mae.ufl.edu
[§] E-mail: wangguoyu@bit.edu.cn

Contract/grant sponsor: NASA Constellation University Institute Program (CUIP)
Contract/grant sponsor: National Natural Science Foundation of China; contract/grant number: 50276004

Received 26 January 2005
Revised 31 May 2005
Accepted 1 June 2005

1. INTRODUCTION

Cavitation occurs in a wide variety of engineering systems: pumps, hydrofoils and underwater bodies. Phenomenologically, cavitation often involves complex interactions of turbulence and phase-change dynamics, large density variation between phases, fast and multiple time scales, and pressure fluctuations. These physical mechanisms are not well understood due to the complex, unsteady flow structures associated with cavitation dynamics and turbulence. There are significant computational issues in regard to stability, efficiency, and robustness of the numerical algorithm for turbulent unsteady cavitating flows.

Noticeable efforts have been made in employing the Navier–Stokes equations for turbulent cavitating flow computations. A review of the representative cavitation models is presented by Wang *et al.* [1]. Among the various modelling approaches, the transport equation-based cavitation models (TEM) have received growing interests, and both steady and unsteady flow computations have been reported [2–11]. In the TEM, a transport equation for either mass or volume fraction, with appropriate source terms to regulate the mass transfer between vapour and liquid phases, is adopted. Taking the advantage of the homogeneous flow theory, the mixture concept is introduced, and a single set of mass and momentum equations along with turbulence and cavitation models is solved in the whole flow field. One apparent advantage of this model comes from the convective character of the equation, which allows modelling of the impact of inertial forces on cavities like elongation, detachment and drift of cavity bubbles [1]. Different modelling concepts embodying qualitatively similar source terms with alternative numerical techniques have been proposed by various researchers [2–5, 9–11]. Numerically, Singhal *et al.* [2] and Senocak and Shyy [7–11] have utilized pressure-based algorithms, while Merkle *et al.* [3] and Kunz *et al.* [4] have employed the artificial compressibility method. Senocak and Shyy [8, 10] and Wu *et al.* [12] have assessed the merits of alternative transport equation-based modelling approaches based on a newly developed interfacial dynamics-based-cavitation model (IDCM) accounting for cavitation dynamics. They have shown that for steady-state computations, various cavitation models produce comparable pressure distributions. In addition, Vaidyanathan *et al.* [13] have performed a sensitivity analysis on a TEM to optimize the coefficients of its source terms. Wu *et al.* [14] have extended the application to 3-D simulations. Senocak and Shyy [9, 11] have used an empirical factor to construct the interfacial velocity in time-dependent simulations of the IDCM. In spite of the good agreement in pressure distributions between models, noticeable differences have been observed in the predicted density field. This implies that the compressibility characteristics embodied in each cavitation model are apparently different. This aspect can be significant in the unsteady flow computations because the speed of sound affects the cavity time-dependent features [9, 11, 15].

Besides the cavitation modelling, the turbulence model can significantly influence the cavitating flow structures. Serious implications of turbulence modelling on cavitating flows were recently revealed by researchers [12, 15–17]. They have reported that high eddy viscosity of the original Launder–Spalding version of the k–ε Reynolds-averaged Navier–Stokes (RANS) model [18] can dampen the vortex shedding motion and excessively attenuate the cavitation instabilities. Consequently, simulation of phenomena such as periodic cavity inception and detachment requires improved modelling approaches. The large eddy simulation (LES) approach, originally proposed by Smagorinsky [19] and refined by many researchers, e.g. References [20–22], is an actively pursued route to simulate turbulent flows. However, it is fundamentally difficult to find a grid-independent LES solution unless one explicitly assigns a filter scale [21], making the state-of-the-art immature for cavitating flow computations. On the other hand, attempts have also been made to employ the information obtained from direct numerical simulations (DNS) to supplement lower order models, e.g. Reference [23]. To our knowledge, no efforts have been reported to employ LES or DNS for turbulent cavitating flows of practical interest.

Recently, efforts have been made to combine the filter concept and the RANS model in single-phase [24–29] and, recently and more preliminarily, cavitating flow [12, 16, 30] computations. For example, Johansen *et al.* [29] have formulated a filter-based model (FBM) to address some of the known deficiencies of the RANS approaches. The new model imposes an independent filter scale, by considering the grid size employed, on the computation of the eddy viscosity. By preventing excessive dissipation incurred in the original k–ε model, the imposed filter allows capturing of flow scales commensurate with the grid resolution while relying on the turbulence closure for the irresolvable scales. This hybrid model has significantly improved the prediction of single-phase flow over a square cylinder. For both single-phase and cavitating flows, the FBM results exhibits a significant reduction in the eddy viscosity and consequently creates more unsteady flow characteristics [12, 16, 29]. Naturally, it will be interesting to systematically investigate the performance of the FBM in cavitating flow computations.

Regarding the IDCM, in our previous efforts [9, 11, 12, 16], the cavity interfacial velocity was linked to the local fluid velocity in the time-dependent computations. Such an approach lacks generality because the interfacial velocity is supposed to be a function of the phase change process. Fundamentally, the interfacial velocity can be accurately estimated based on the moving boundary computational techniques [31]. In the present study, a simplified approach is taken by accounting for the phase transformation process in each computational cell. Combining the IDCM for cavitation and the FBM for RANS turbulence model, we have made a systematic investigation of time-dependent turbulent cavitating flow over a Clark-Y hydrofoil, based on the experimental observation [1].

In the present efforts, we investigate the interplay between turbulence and cavitation models. Specifically, the IDCM is combined with either the original Launder–Spalding or filter-based k–ε model in time-dependent computations for 2-D cavitating flow over the Clark-Y hydrofoil for the Reynolds number of $Re = 7.0 \times 10^5$, at two angles-of-attack (AoA) of 5 and 8°. At AoA = 8°, the cavitation number ranges from 2.50 to 0.80. At AoA = 5°, the cavitation number is ranging from 2.02 to 0.55. These parameters cover no-cavitating, inception, sheet and cloud cavitating flow regimes. The assessment of the cavitation and turbulence models is evaluated by comparing the numerical results with the experimental information. In the following, we first summarize the essential elements of the governing equations, the modelling concepts, and the numerical techniques, then present the results from both computational and experimental efforts.

2. THEORETICAL FORMULATION

2.1. Favre-averaged continuity and momentum equations

The set of governing equations comprises the conservative form of the density-averaged Navier–Stokes equations, coupling with cavitation model and the k–ε two-equation turbulence closure. The continuity, momentum equations in the Cartesian co-ordinates are given below:

$$\frac{\partial \rho_m}{\partial t} + \frac{\partial(\rho_m u_i)}{\partial x_i} = 0 \tag{1}$$

$$\frac{\partial(\rho_m u_i)}{\partial t} + \frac{\partial(\rho_m u_i u_j)}{\partial x_j} = -\frac{\partial p}{\partial x_i} + \frac{\partial}{\partial x_j}\left[(\mu + \mu_t)\left(\frac{\partial u_i}{\partial x_j} + \frac{\partial u_j}{\partial x_i} - \frac{2}{3}\frac{\partial u_k}{\partial x_k}\delta_{ij}\right)\right] \tag{2}$$

where ρ_m is the mixture density, u is the velocity, p is the pressure, μ and μ_t are the laminar and turbulent viscosity, and subscripts i, j, k are the axes directions, respectively.

2.2. Interfacial dynamics-based cavitation model

Based on the homogeneous equilibrium flow theory, without accounting for the thermal energy and nonequilibrium-phase change effects, a volume fraction transport equation to account for the cavitation dynamics is present as

$$\frac{\partial \alpha_L}{\partial t} + \nabla \cdot (\alpha_L \mathbf{u}) = \dot{m}^+ + \dot{m}^- \tag{3}$$

$$\rho_m = \rho_L \alpha_L + \rho_V (1 - \alpha_L) \tag{4}$$

where α_L is the liquid volume fraction, $\dot{m}^+$ and $\dot{m}^-$ are source terms for condensation and evaporation. ρ_L and ρ_V are the liquid and vapour density.

The source terms $\dot{m}^+$ and $\dot{m}^-$ in the IDCM, originally proposed by Senocak and Shyy [8–11], are derived by considering the mass and normal momentum conservation at the liquid–vapour interface, neglecting the surface tension and buoyancy effects for the typical situation of large Weber and Froude numbers. They are given as follows:

$$\begin{aligned} \dot{m}^- &= \frac{\rho_L \alpha_L \,\mathrm{Min}(0, p - p_V)}{\rho_V (V_{V,n} - V_{I,n})^2 (\rho_L - \rho_V) t_\infty} \\ \dot{m}^+ &= \frac{(1 - \alpha_L)\mathrm{Max}(0, p - p_V)}{(V_{V,n} - V_{I,n})^2 (\rho_L - \rho_V) t_\infty} \end{aligned} \tag{5}$$

with the vapour-phase normal velocity $V_{V,n}$ and interfacial velocity $V_{I,n}$, $t_\infty = c/U_\infty$ is the time scale, c is the hydrofoil chord and U_∞ is the inlet velocity. Generally, the normal velocity of the interface, $V_{I,n}$ is not equal to that of the liquid-phase velocity $V_{L,n}$. Under the steady state, $V_{I,n}$ is equal to zero. In the case of $p = p_v$, $\dot{m}^+ = 0$ and $\dot{m}^- = 0$.

In the current study, we estimate the interfacial velocity via an approximate procedure. By integrating Equation (5) through the control volume, we have $\dot{m}^+ \cdot \Delta V$ and $\dot{m}^- \cdot \Delta V$. The net interface velocity (the interface velocity relative to the local flow field) becomes

$$\begin{aligned} V_{I,n}^{\mathrm{net}} A &= \Delta \dot{m} \\ V_{I,n}^{\mathrm{net}} &= \frac{\Delta \dot{m}}{A} = \frac{\mathrm{abs}(\dot{m}^+ \Delta V) - \mathrm{abs}(\dot{m}^- \Delta V)}{A} \end{aligned} \tag{6}$$

where A is the interface area between vapour and liquid phases.

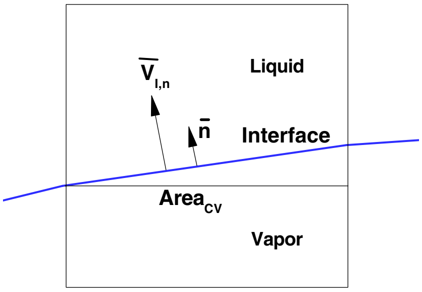

Figure 1. Interface vector sketch in a CV.

Practically, the control volume face area, Area_{CV}, is projected to the interface normal direction, which can be obtained by taking the gradient of the volume fraction, denoted as S, as shown in Figure 1 for the 2-D situation:

$$\begin{aligned} \mathbf{n} &= \frac{\nabla \alpha_{\text{L}}}{|\nabla \alpha_{\text{L}}|} = n_x \mathbf{i} + n_y \mathbf{j} \\ S &= \frac{\text{Area}_{\text{CV}}}{|n_x/\sqrt{n_x^2 + n_y^2}|} \end{aligned} \tag{7}$$

Substituting S into Equation (6) leads to:

$$V_{\text{I},n}^{\text{net}} = \frac{\Delta \dot{m}}{S} = \frac{\text{abs}(\dot{m}^{+} \Delta V) - \text{abs}(\dot{m}^{-} \Delta V)}{S} \tag{8}$$

The interface velocity includes two parts: flow field local velocity $V_{\text{I},n}^{\text{Local}} = V_{\text{V},n}$ and net velocity $V_{\text{I},n}^{\text{net}}$. Then we can have the following derivation:

$$(V_{v,n} - V_{\text{I},n})^2 = [V_{v,n} - (V_{\text{I},n}^{\text{net}} + V_{\text{I},n}^{\text{Local}})]^2 = (V_{\text{I},n}^{\text{net}})^2 \tag{9}$$

Finally, the source terms assume the format shown below:

$$\begin{aligned} \dot{m}^{-} &= \frac{\rho_{\text{L}} \alpha_{\text{L}} \,\text{Min}(0, p - p_{\text{V}})}{\rho_{\text{V}} (V_{\text{I},n}^{\text{net}})^2 (\rho_{\text{L}} - \rho_{\text{V}}) t_{\infty}} \\ \dot{m}^{+} &= \frac{(1 - \alpha_{\text{L}}) \text{Max}(0, p - p_{\text{V}})}{(V_{\text{I},n}^{\text{net}})^2 (\rho_{\text{L}} - \rho_{\text{V}}) t_{\infty}} \end{aligned} \tag{10}$$

2.3. Turbulence model

2.3.1. The Launder and Spalding k–ε turbulence model (*LSM*). The k–ε turbulence model originally presented by Launder and Spalding [18] is as follows:

$$\frac{\partial (\rho_m k)}{\partial t} + \frac{\partial (\rho_m u_j k)}{\partial x_j} = p - \rho_m \varepsilon + \frac{\partial}{\partial x_j} \left[\left(\mu + \frac{\mu_t}{\sigma_k} \right) \frac{\partial k}{\partial x_j} \right] \tag{11}$$

$$\frac{\partial(\rho_m \varepsilon)}{\partial t} + \frac{\partial(\rho_m u_j \varepsilon)}{\partial x_j} = C_{\varepsilon 1} \frac{\varepsilon}{k} P_t - C_{\varepsilon 2} \rho_m \frac{\varepsilon^2}{k} + \frac{\partial}{\partial x_j}\left[\left(\mu + \frac{\mu_t}{\sigma_\varepsilon}\right)\frac{\partial \varepsilon}{\partial x_j}\right] \tag{12}$$

where k and ε are turbulent kinetic energy and dissipation rate, respectively.

The turbulent energy production, the Reynolds stress tensor terms, and the Boussinesq sub-filter viscosity are defined as follows:

$$\begin{gathered} P_t = \tau_{ij} \frac{\partial u_i}{\partial x_j}, \quad \tau_{ij} = -\overline{\rho u'_j u'_j} \\ \overline{u'_j u'_j} = \frac{2k\delta_{ij}}{3} - v_t \left(\frac{\partial u_j}{\partial x_i} + \frac{\partial u_i}{\partial x_j}\right) \end{gathered} \tag{13}$$

The parameters adopted in this model are $C_{\varepsilon 1} = 1.44$, $C_{\varepsilon 2} = 1.92$, $\sigma_\varepsilon = 1.3$, $\sigma_k = 1.0$. The turbulent viscosity is defined as

$$\mu_t = \frac{\rho_m C_\mu k^2}{\varepsilon}, \quad C_\mu = 0.09 \tag{14}$$

2.3.2. An FBM for turbulence closure. In Johansen *et al.*'s [29] approach, the original k–ε equations are still employed; however, the turbulent viscosity is computed with a filtering procedure:

$$\mu_t = \frac{\rho_m C_\mu k^2}{\varepsilon} F, \quad C_\mu = 0.09 \tag{15}$$

where F is the filter function defined in terms of the ratio of filter size (Δ) and the turbulent length scale:

$$F = \mathrm{Min}\left[1, c_3 \frac{\Delta \varepsilon}{k^{3/2}}\right] \tag{16}$$

As pointed out by Johansen *et al.* [29], the proposed filter, as in Equation (16), will recover the Launder and Spalding k–ε model for a very coarse filter size, i.e. when we practically stop filtering. Furthermore, next to the solid wall, the chosen filter returns $F = 1$ and the wall function is adopted.

3. NUMERICAL METHODS

The present Navier–Stokes solver employs pressure-based algorithms and the finite volume approach [32–34]. The governing equations are solved on a multi-block structured curvilinear grid system. Because the properties sharply change across the liquid–vapour boundaries, the computational algorithms of single-phase, low Mach number flow often meet serious convergence and stability problems for cavitating flows. To facilitate time-dependent computations, an extended PISO algorithm [34] is coupled with the pressure-based method for cavitating flow through predictor-correction steps. The pressure-based methods for steady computations of turbulent cavitating flows are described in Reference [7], which employed an upwind-biased flux computation procedure. To improve the numerical performance in time-dependent computations, a differencing procedure approximating the definition of speed of sound is employed [9, 11].

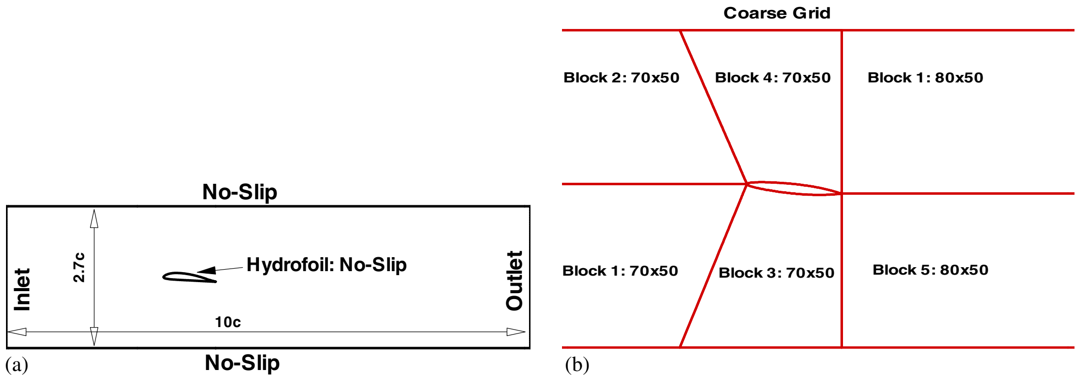

Figure 2. Geometry sketch and grid blocks: (a) geometry configuration and boundary conditions, c is the hydrofoil chord; and (b) grid blocks and coarse grid numbers.

For the computational set-up, as shown in Figure 2(a), the computational domain and boundary conditions are given according to the experimental set-up. The Clark-Y hydrofoil is located at the water tunnel centre. The two AoA considered are 5 and 8°. The hydrofoil chord is c and the hydrofoil leading edge is $3c$ away from the inlet. The two important parameters are Reynolds number, and cavitation number based on the inlet pressure P_∞ and the vapour pressure P_v with inlet velocity U_∞:

$$Re = \frac{U_\infty c}{\nu} = 7 \times 10^5 \tag{17}$$

$$\sigma = \frac{P_\infty - P_v}{\rho U_\infty^2/2} \tag{18}$$

The filter size in the present study is chosen to be larger than the largest grid scale employed in the computation, namely, $\Delta \geqslant \max(\sqrt{\Delta x \cdot \Delta y})$ and is set to be $\Delta = 0.08c$.

Computations have been done for two AoA and several cavitation numbers. Specifically, for $\text{AoA} = 5°$ under four flow regimes: no-cavitation ($\sigma = 2.02$), inception ($\sigma = 1.12$), sheet cavitation ($\sigma = 0.92$), and cloud cavitation ($\sigma = 0.55$), and $\text{AoA} = 8°$ under three cavitation numbers: no-cavitation ($\sigma = 2.50$), sheet cavitation ($\sigma = 1.40$), cloud cavitation ($\sigma = 0.80$). All cases above are at the same Reynolds number $Re = 7 \times 10^5$.

As mentioned, two different turbulence models, LSM and FBM, have been employed to help probing the characteristics of cavitation and turbulence modelling interactions. The outlet pressure is fixed and adjustment of the vapour pressure is needed to be consistent with the prescribed cavitation number in each case.

4. RESULTS AND DISCUSSION

4.1. *Grid sensitivity analysis*

To investigate the grid dependency, two grids are adopted in the computation: coarse grid and fine grid. The grid blocks and numbers of the coarse grid are given in Figure 2(b).

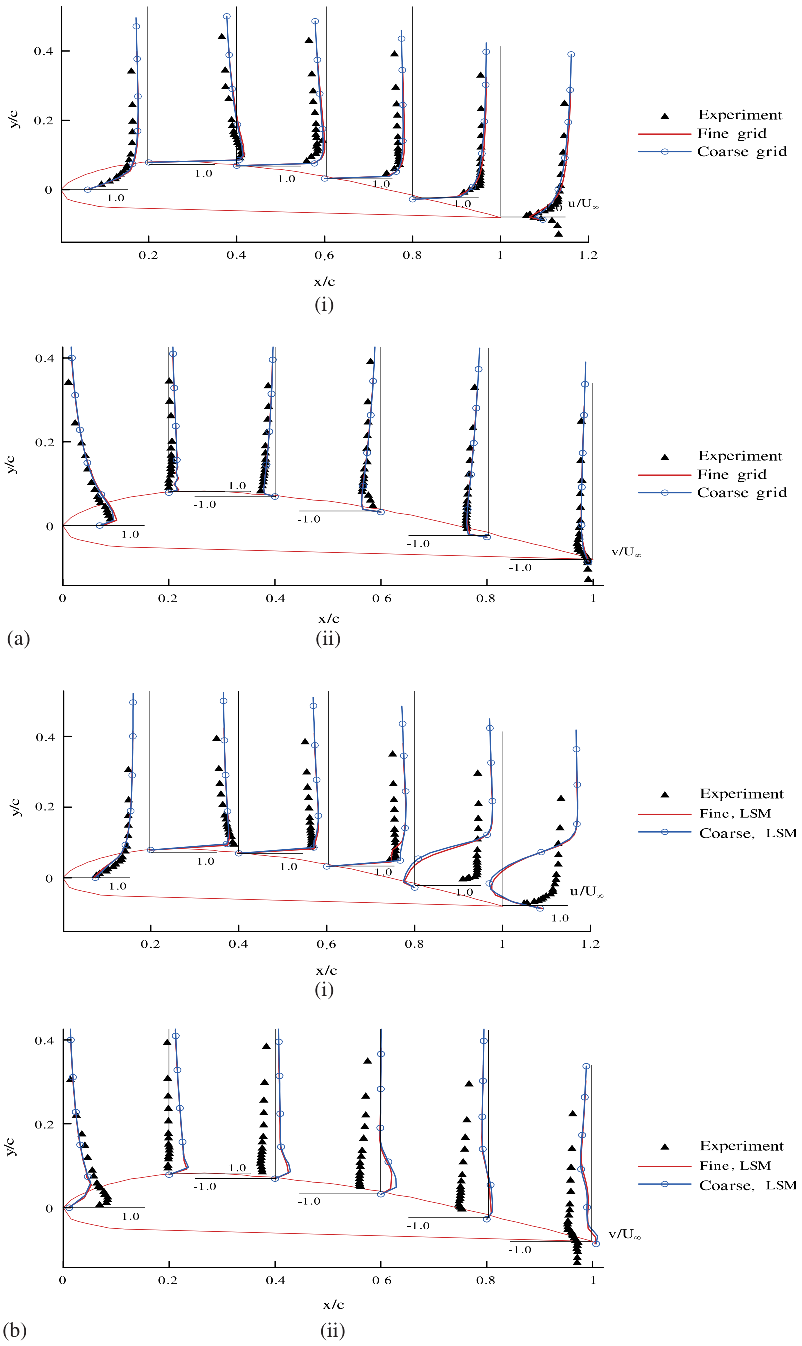

Figure 3. Time-averaged velocity comparisons between coarse and fine grids, LSM, AoA = 5°. Experimental data are from Reference [1]: (a) no-cavitation, $\sigma = 2.02$. (i) u velocity, (ii) v velocity; and (b) cloud cavitation, $\sigma = 0.55$. (i) u velocity, (ii) v velocity.

The fine grid has 60% more number of nodes than that of the coarse grid on the vertical direction while maintaining the same distribution on the horizontal direction. Two different cavitation numbers, $\sigma = 2.02$ and 0.55, both at AoA $= 5^\circ$ have been investigated. Overall, the solutions on both grids are in good agreement. The time-averaged u and v velocity profiles with $\sigma = 2.02$ and 0.55 using the LSM are shown in Figure 3. The results based on the FBM are of similar nature and will not be repeated.

Hereafter, to reduce the cost of time-dependent computations, we use the coarse grid in the computations.

4.2. *Visualization of cavity and flow field*

First, we focus on the LSM results to analyse the performance of the IDCM. Figures 4 and 5 show the time-averaged flow structure and cavity shape under varied cavitation numbers. With no cavitation, the flow field is attached without separation for both AoA $= 5$ and 8°, see Figures 4(a, left) and 5(a, left). This is consistent with the experimental observation. With cavitation, the density changes by a factor of 1000 between liquid and vapour phase. Consequently, there is a drastic reduction in the amount of mass inside the cavity, and a contraction of the fluid flow behind the cavity. With the reduction of the cavitation number, the cavitating cavity and recirculation zone become bigger. At cloud cavitation, the cavity experiences shedding, causing multiple recirculating flows, see Figures 4(d, left) and 5(c, left). Compared to the experimental data, as shown in Tables I and II, for both AoA, the predicted cavity sizes demonstrate qualitatively consistent rending, albeit generally over-predicted. For incipient cavitation, the experiment observed the recurring formation of hair-pin type of cavitating vortex structures, which are not attached to the solid surface [1]. This type of flow structure is not captured in the computation. The time-averaged flow structures associated with sheet and cloud cavitation, on the other hand, seem to be reasonably captured computationally. Furthermore, the time-averaged outcome of employing both LSM and FBM seems compatible.

The temporal evolution of the computed and experimentally observed flow structures with cloud cavitation, under two AoA, are shown in Figures 6 and 7. Figure 6(a, left) shows the sequence of flow structures predicted by LSM at AoA $= 5^\circ$. The corresponding flow predicted by the FBM is shown on the right column. The experimental visual image is shown in Figure 6(b). The flow structures at AoA $= 8^\circ$ are shown in Figure 7. Both computations and experiment indicate that as the AoA increases, the cavity exhibits more pronounced recurrence of the size variation. The FBM predicts stronger time-dependency than the LSM. We will further investigate this aspect in the following discussion. To help elucidate the main features of the cavity dynamics from both numerical and experimental studies, we show in Figure 8 three stages of the cavity sizes, for cloud cavitation $\sigma = 0.55$ at AoA $= 8^\circ$. The figure demonstrates that the numerical simulation is capable of capturing the initiation of the cavity, growth toward trailing edge, and subsequent shedding, in accordance with the qualitative features observed experimentally.

4.3. *Velocity profiles and lift/drag coefficients*

The mean horizontal (u) and vertical (v) velocities of the flow field are illustrated in Figures 9 (AoA $= 5^\circ$) and 10 (AoA $= 8^\circ$). The time-averaged velocity profiles are documented at six chordwise locations, 0, 20, 40, 60, 80, and 100% of the leading edge, under different

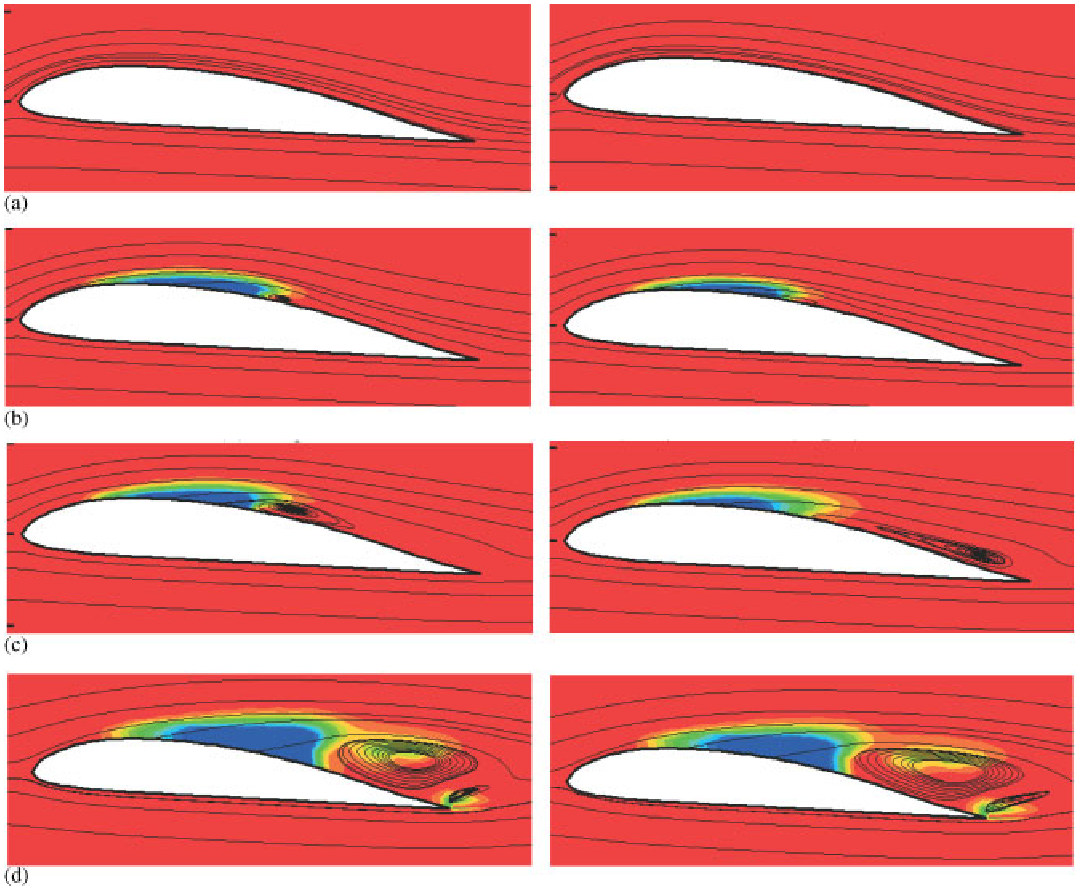

Figure 4. Time-averaged volume fraction contours and streamlines, AoA = 5°: (a) no-cavitation, $\sigma = 2.02$: LSM (left) and FBM (right); (b) incipient cavitation, $\sigma = 1.12$: LSM (left) and FBM (right); (c) sheet cavitation, $\sigma = 0.92$: LSM (left) and FBM (right); and (d) cloud cavitation, $\sigma = 0.55$: LSM (left) and FBM (right).

cavitation numbers. With no cavitation, the numerical results agree well with the experiment, and the results of the two turbulence models are virtually identical, as shown in Figures 9(a) and 10(a). With the cavitation number decreasing, the differences between prediction and measurement become more substantial, especially at the cavity closure region. Overall, considering the difficulties in experimental measurement [1] the agreement is reasonable.

Figure 11 shows the time-averaged lift and drag coefficients collected from experiment and computations. The computational models estimate that as cavitation appears the lift decreases. However, experimentally, such a drop does not take place until the sheet cavitation regime. For sheet and cloud cavitation, both computations and experiment show consistent trends, namely, marked reduction in lift as the cavitation becomes more pronounced. From the time-averaged flow structures shown earlier, one clearly sees that the cavity changes the effective

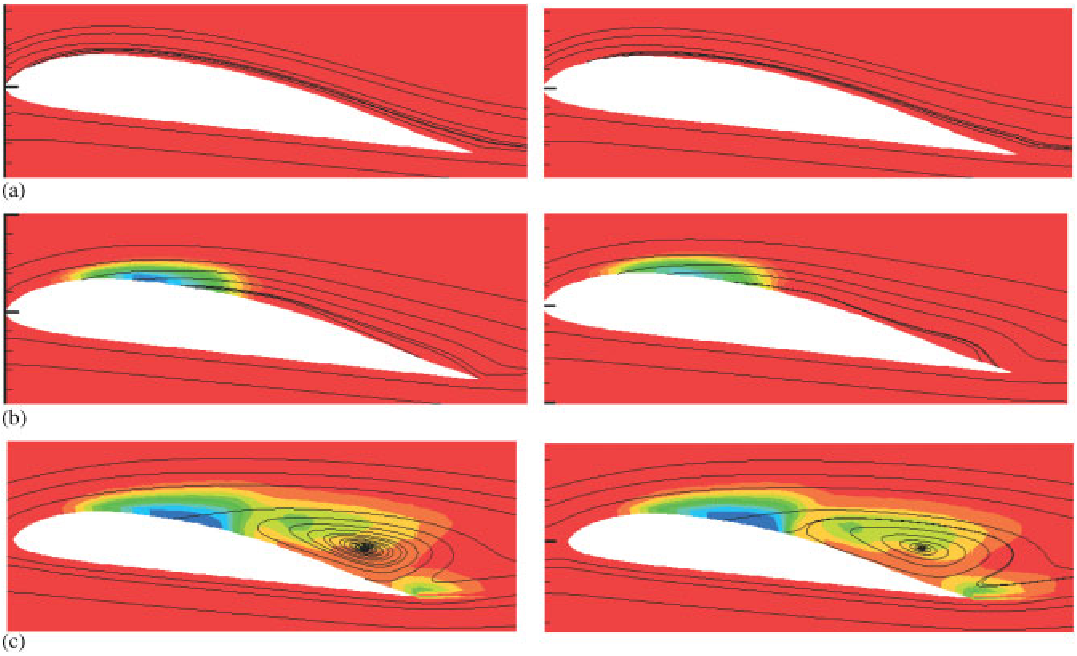

Figure 5. Time-averaged volume fraction contours and streamlines, AoA = 8°: (a) no-cavitation, $\sigma = 2.50$: LSM (left) and FBM (right); (b) sheet cavitation, $\sigma = 1.40$: LSM (left) and FBM (right); and (c) cloud cavitation, $\sigma = 0.80$: LSM (left) and FBM (right).

Table I. Time-averaged cavity leading and trailing positions ($\alpha_L = 0.95$ as cavity boundary), AoA = 5°.

	Inception, $\sigma = 1.12$			Sheet cavitation, $\sigma = 0.92$			Cloud cavitation, $\sigma = 0.55$		
Position	LSM	FBM	Exp.	LSM	FBM	Exp.	LSM	FBM	Exp.
Leading	0.13	0.13	—	0.13	0.13	0.23	0.16	0.17	0.22
Trailing	0.62	0.57	—	0.64	0.64	0.68	1.01	1.04	0.90

Table II. Time-averaged cavity leading and trailing positions ($\alpha_L = 0.95$ as cavity boundary), AoA = 8°.

	Sheet cavitation, $\sigma = 1.40$			Cloud cavitation, $\sigma = 0.80$		
Position	LSM	FBM	Exp.	LSM	FBM	Exp.
Leading	0.094	0.098	0.15	0.12	0.13	0.15
Trailing	0.53	0.52	0.56	1.07	1.10	0.84

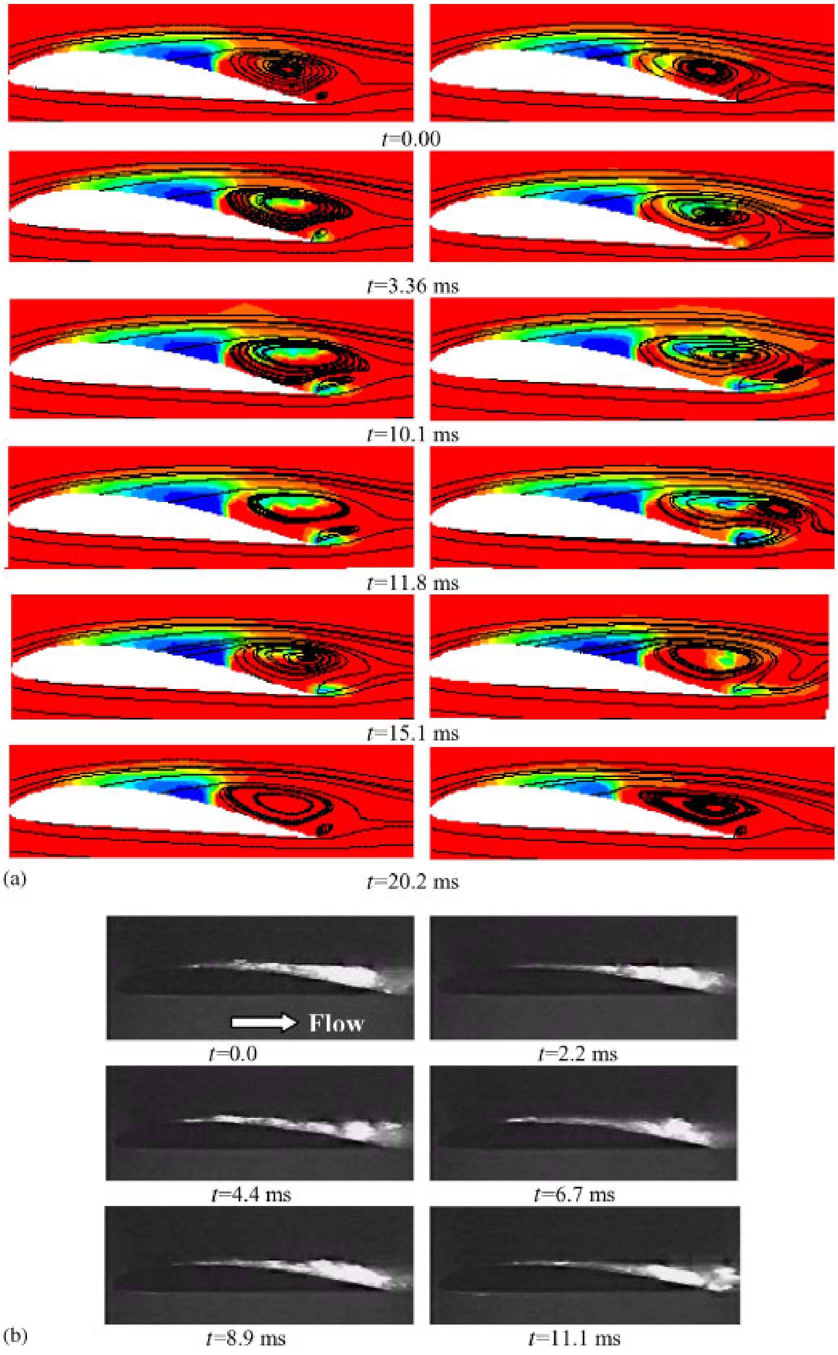

Figure 6. Time evolutions of cloud cavitation, $\sigma = 0.55$, $\mathrm{AoA} = 5°$: (a) numerical results of two turbulent models: LSM (left) and FBM (right); and (b) side views of the experimental visual from Reference [1].

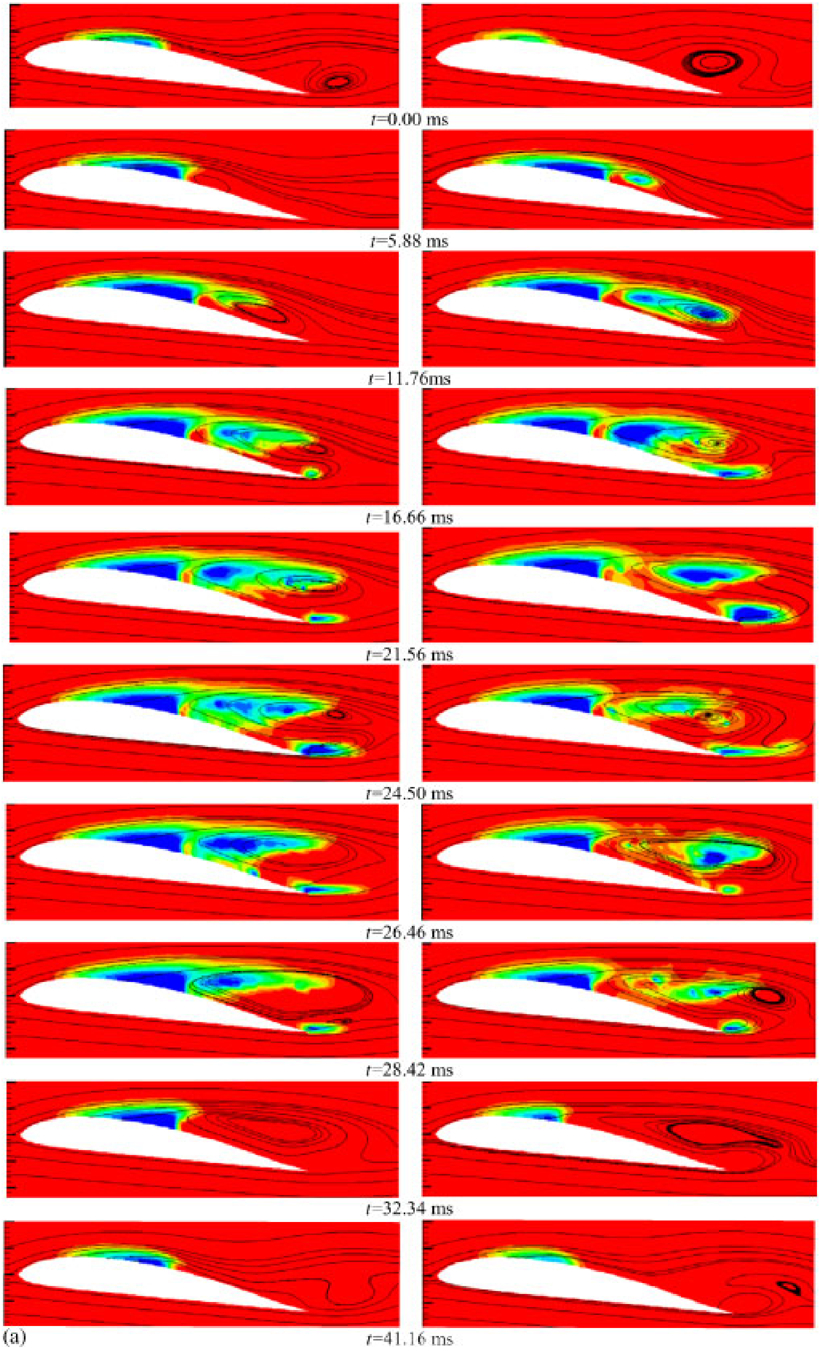

Figure 7. Time evolutions of cloud cavitation, $\sigma = 0.80$, AoA $= 8°$: (a) numerical results of two turbulence models: LSM (left) and FBM (right); and (b) side views of the experiment visual from Reference [1].

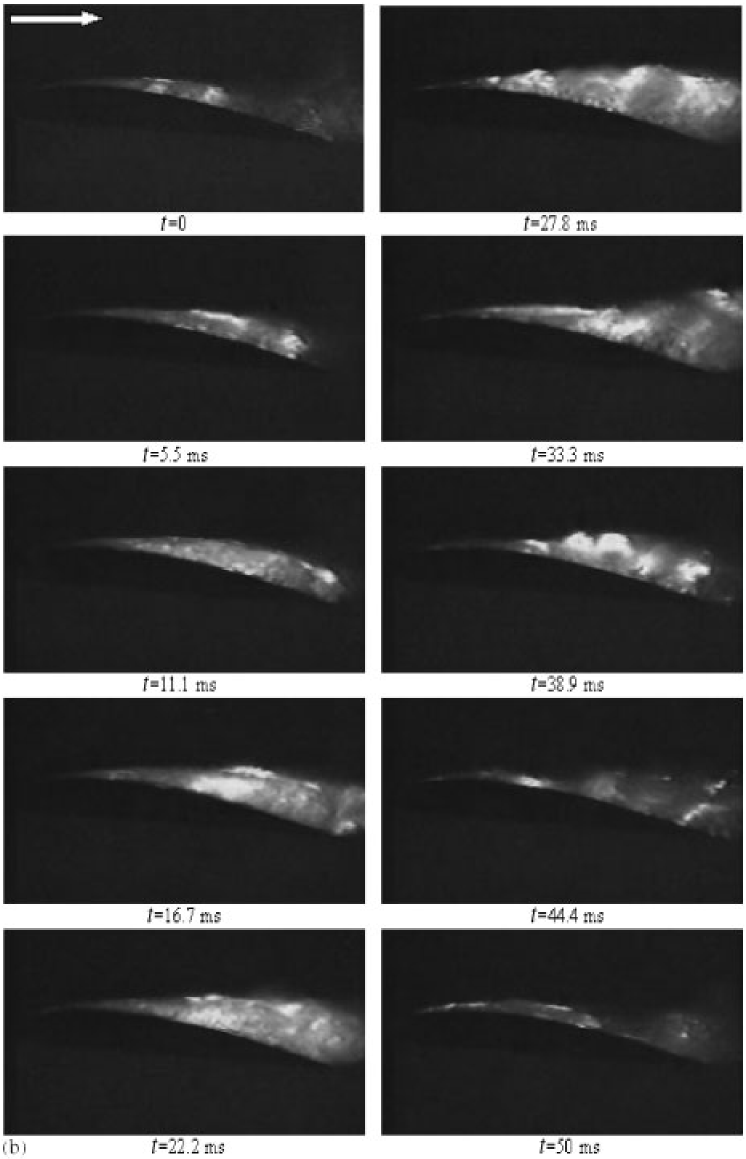

Figure 7. *Continued.*

shape of the hydrofoil, causing flow to separate. Hence, the reduction in lift is expected. Regarding the drag coefficient, there is a marked increase from sheet to cloud cavitation, which is reflected by the computational models. Overall, the lift coefficient is under-predicted and drag coefficient is over-predicted by both turbulence models, but the trends are reasonably captured in the sheet and cloud cavitation regimes.

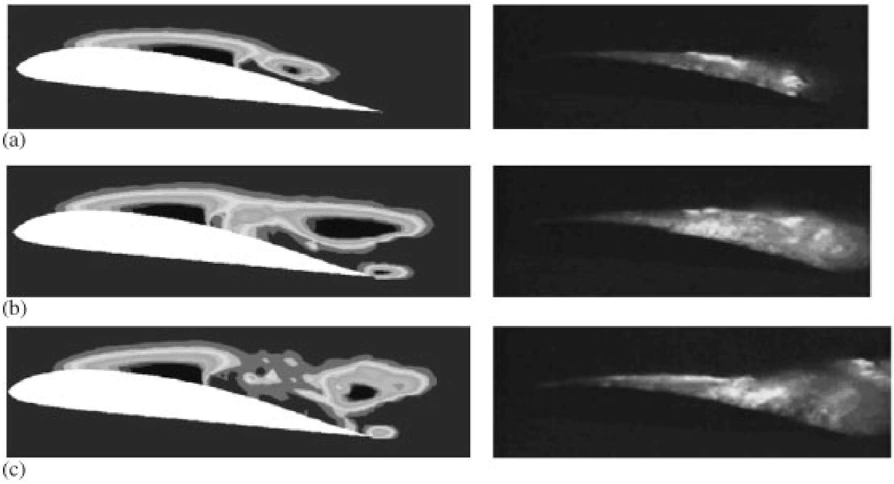

Figure 8. Cavity stage comparisons, $\sigma = 0.80$, AoA = 8°. Experiment visuals are from Reference [1]: (a) early stage: cavity formation, FBM (left) and experiment (right); (b) second stage: cavity growth toward trailing edge, FBM (left) and experiment (right); and (c) third stage: cavity break-up and shedding, FBM (left) and experiment (right).

4.4. Assessment of IDCM parameters

To better understand the IDCM performance, we examine the condensation $\dot{m}^+$ and evaporation $\dot{m}^-$ source terms. A TEM cavitation model heuristically developed by Merkle *et al.* [3] and extensively applied by Ahuja *et al.* [5] show identical model equations with the source terms given as

$$\begin{aligned} \dot{m}^- &= \frac{C_{\mathrm{dest}}\rho_{\mathrm{L}}\alpha_{\mathrm{L}}\,\mathrm{Min}(0, p - p_{\mathrm{V}})}{\rho_{\mathrm{V}}(\rho_{\mathrm{L}}U_\infty^2/2)t_\infty} \\ \dot{m}^+ &= \frac{C_{\mathrm{prod}}(1-\alpha_{\mathrm{L}})\mathrm{Max}(0, p - p_{\mathrm{V}})}{(\rho_{\mathrm{L}}U_\infty^2/2)t_\infty} \end{aligned} \tag{19}$$

In the published applications [3] $C_{\mathrm{dest}} = 1.0$ and $C_{\mathrm{prod}} = 80$ are often adopted. To compare the IDCM with Merkle *et al.*'s model, we can rearrange Equation (10) following the format of Equation (19) and show that the equivalent model parameters C'_{dest} and C'_{prod} are

$$C'_{\mathrm{dest}} = C'_{\mathrm{prod}} = \frac{0.5\rho_{\mathrm{L}}U_\infty^2}{(\rho_{\mathrm{L}} - \rho_{\mathrm{V}})(V_{\mathrm{I},n}^{\mathrm{net}})^2} \tag{20}$$

Using the solutions obtained at AoA = 5° presented in Figures 4 and 6, we make the following observations:

(1) With the decrease of cavitation number from no-cavitation to cloud cavitation, $C'_{\mathrm{dest}}/C_{\mathrm{dest}}$ varies from $O(10)$ to $O(100)$, and $C'_{\mathrm{prod}}/C_{\mathrm{prod}}$ varies from $O(1)$ to $O(10)$, exhibiting substantial variations in accordance with the cavitation regimes.

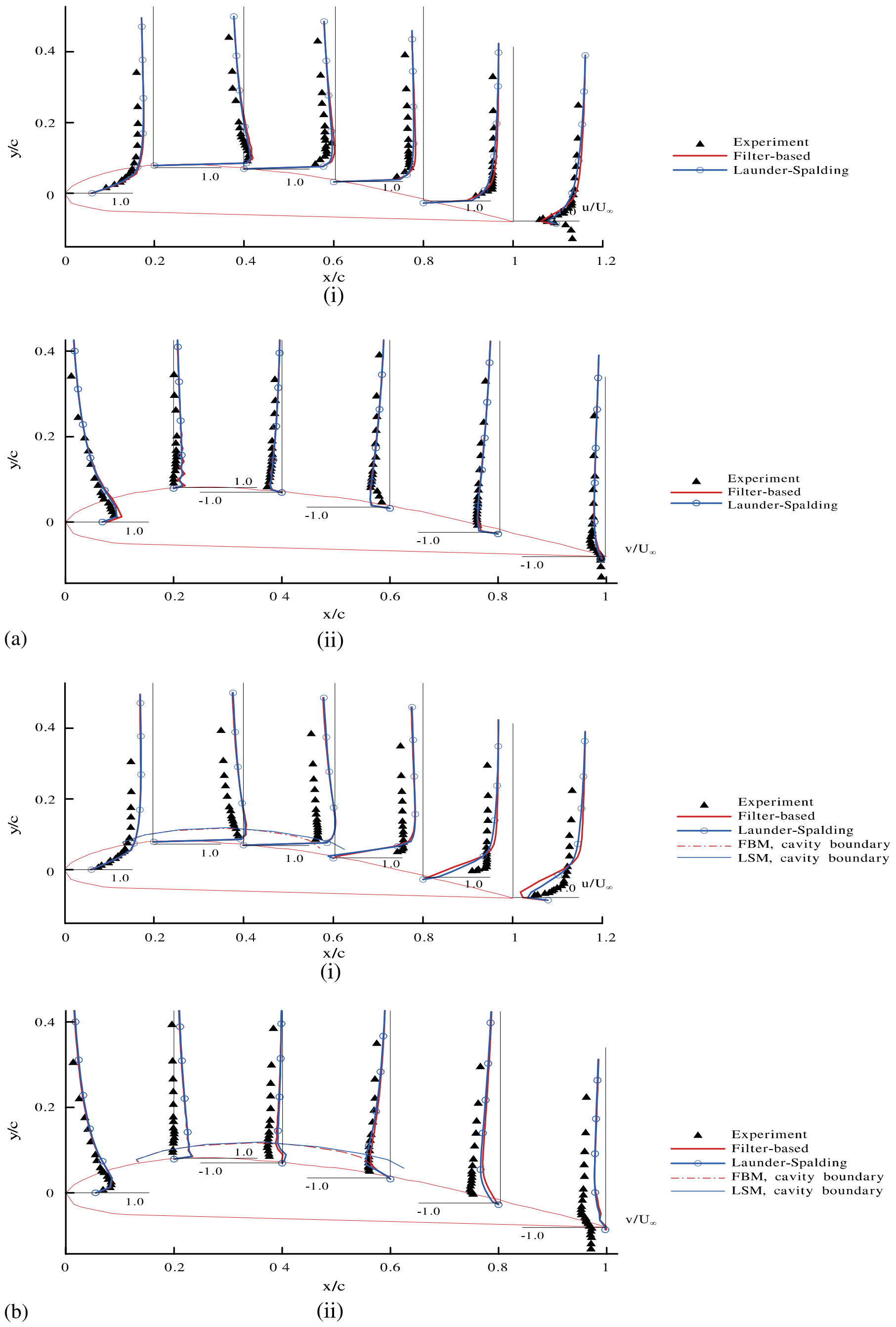

Figure 9. Time-averaged velocities of two turbulence models, AoA = 5°. Exp. data are from Reference [1]: (a) no-cavitation, $\sigma = 2.02$. (i) u velocity, (ii) v velocity; (b) inception, $\sigma = 1.12$. (i) u velocity, (ii) v velocity; (c) sheet cavitation, $\sigma = 0.92$. (i) u velocity, (ii) v velocity; and (d) cloud cavitation, $\sigma = 0.55$. (i) u velocity, (ii) v velocity.

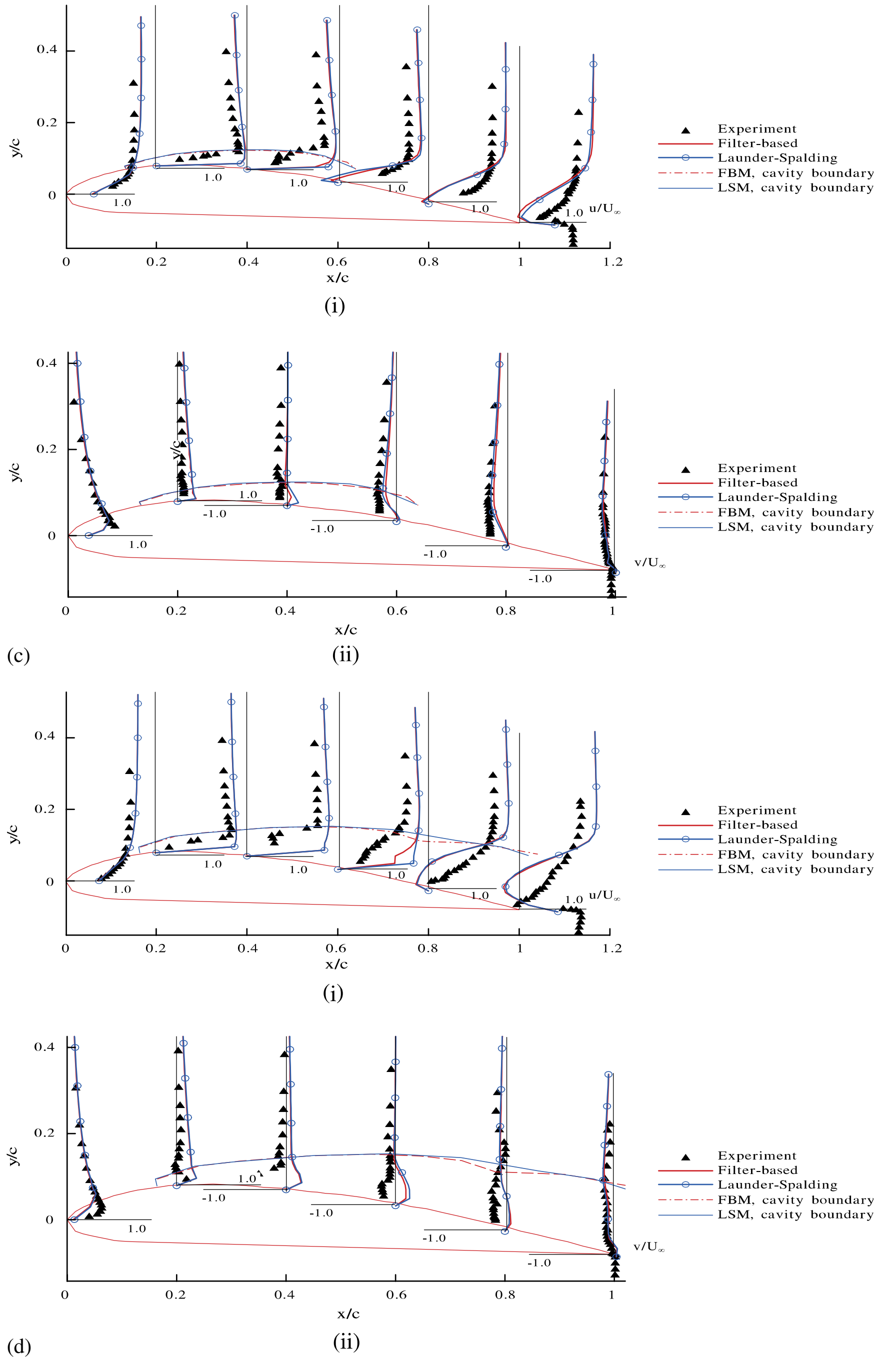

(i)

(c) (ii)

(i)

(d) (ii)

Figure 9. *Continued.*

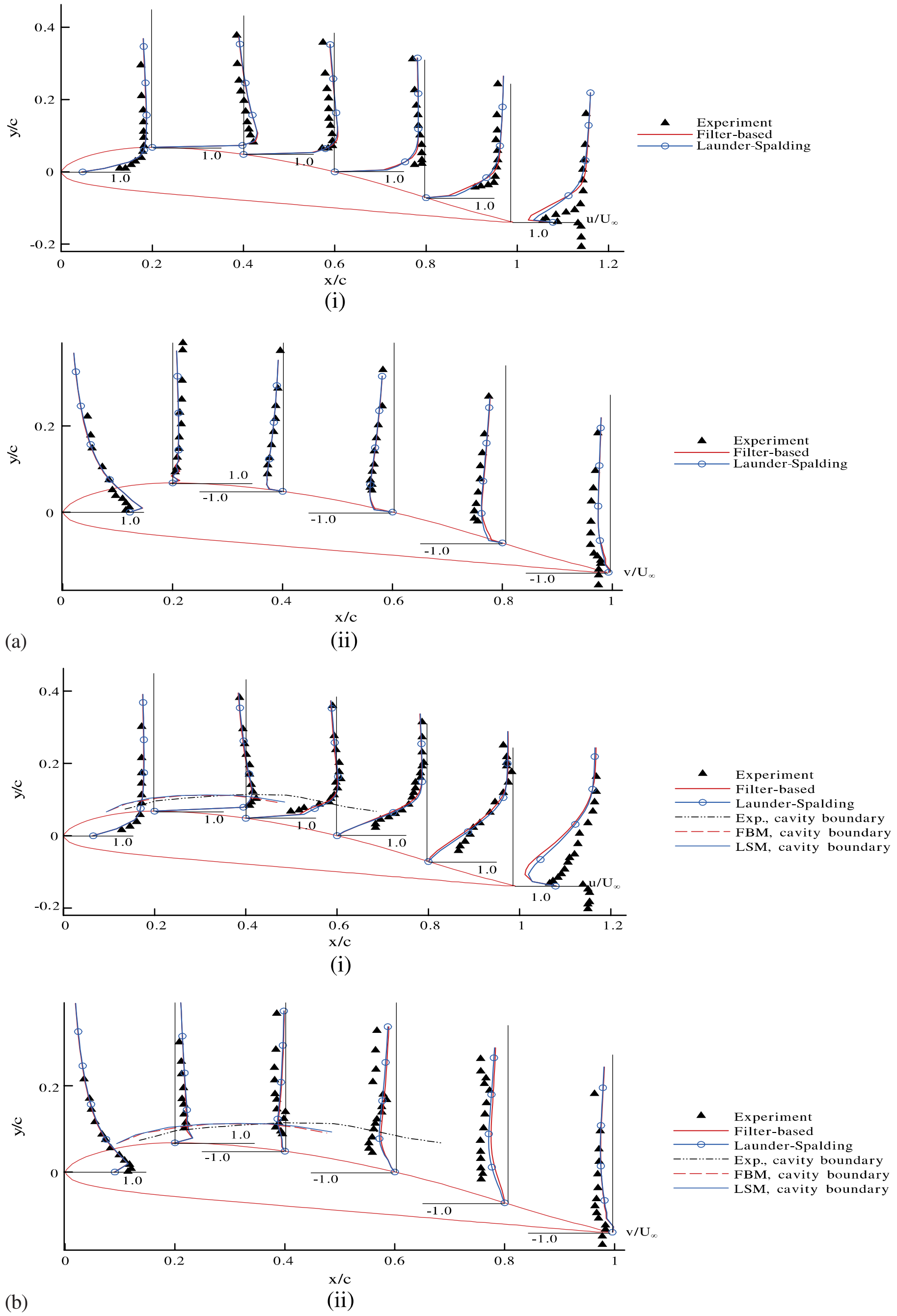

Figure 10. Time-averaged velocities of two turbulence models, AoA = 8°. Exp. data are from Reference [1]: (a) no-cavitation, $\sigma = 2.50$. (i) u velocity, (ii) v velocity; (b) sheet cavitation, $\sigma = 1.40$. (i) u velocity, (ii) v velocity; and (c) cloud cavitation, $\sigma = 0.80$. (i) u velocity, (ii) v velocity.

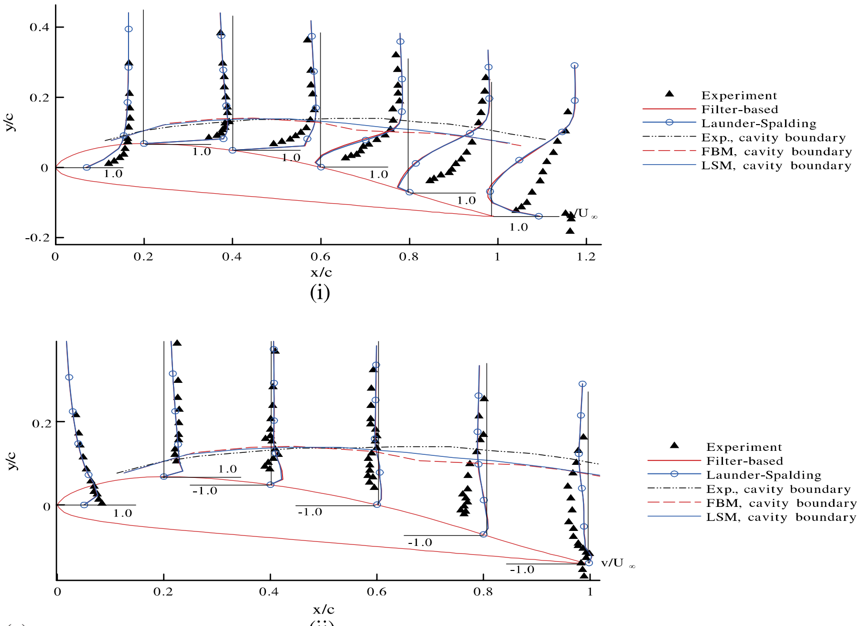

(i)

(c) (ii)

Figure 10. *Continued.*

(2) For a given cavitating flow regime, the variation of ratios $C'_{\mathrm{dest}}/C_{\mathrm{dest}}$ and $C'_{\mathrm{prod}}/C_{\mathrm{prod}}$ for time-averaged results is not much along a constant volume fraction contour. Approximately, they can be considered as unchanged.

(3) The values of C'_{dest} and C'_{prod} experience temporal variations in each cavitation regime. The ratio of $C'_{\mathrm{dest\_max}}/C'_{\mathrm{dest\_min}}$ tends to be $O(1)$–$O(10)$ at the same location inside the cavity, with $C'_{\mathrm{dest\_max}}$ denoting the value at maximum cavity size and $C'_{\mathrm{dest\_min}}$ at minimum cavity size. The investigation on the FBM results shows that the $C'_{\mathrm{dest}}(C'_{\mathrm{prod}})$ has larger temporal fluctuation than the LSM between the maximum and minimum cavity sizes.

Venkateswaran *et al.* [6] stated that the choice of C_{dest} and C_{prod} for steady computations is not critical. However, the same apparently does not hold for time-dependent computations.

4.5. Turbulence models comparison

To assess the turbulence models' performance, we compare the results of the LSM and FBM in each same cavitation flow regime. For no-cavitation, the LSM and FBM exhibit very agreeable time-averaged solutions. As the cavitation number is reduced, the difference becomes more noticeable. With cavitation, the FBM results give a larger wake, especially for sheet cavitation (comparing Figures 4 and 5, left and right columns). Nevertheless, the performance of both turbulence models is largely consistent.

The difference between the FBM and LSM can be illustrated more clearly by the time-dependent results. As already discussed, for cloud cavitation, the cavity breakup phenomenon is more pronounced using the FBM than using the LSM in the cavity time evolutions in

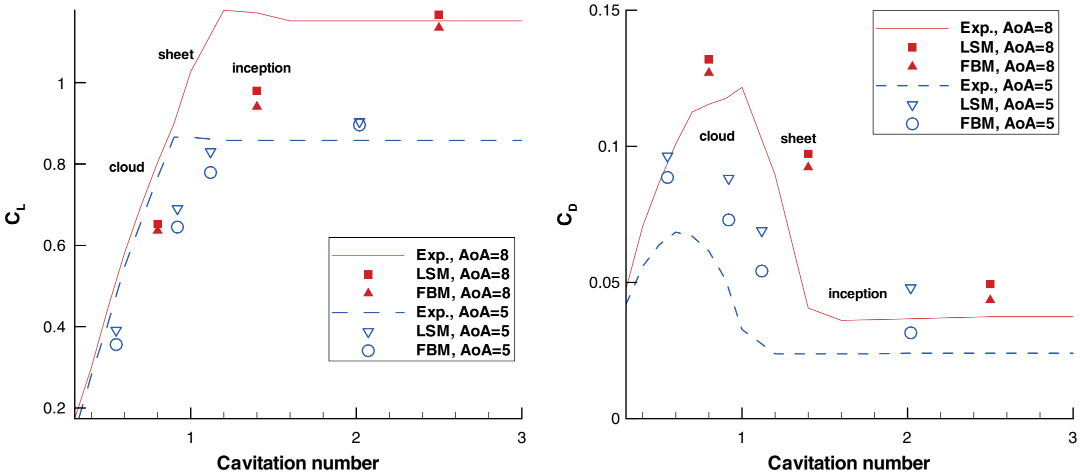

Figure 11. Time-averaged lift and drag coefficients comparisons. Exp. data are from Reference [1].

Figures 6 and 7. In Figure 12, we also compare the time-averaged eddy viscosity distributions yielded by both turbulence models, with different cavitation numbers at AoA = 5°. With both turbulence models, we observe that the eddy viscosity decreases as the cavitation becomes more pronounced and fluctuating in time. Furthermore, the eddy viscosity increases in the recirculation region. It is also clear that the LSM yields consistently higher eddy viscosity, resulting in reduced unsteadiness of the computed flow field.

5. CONCLUSIONS

A filtered Navier–Stokes model, originated from the standard k–ε turbulence model, is applied to turbulent cavitating flows in time-dependent computations, coupled with a recently developed IDCM. Based on the net transformation rate between phases, a new approximation is adopted to evaluate the interfacial velocity. The numerical results qualitatively agree with the experimental data. Based on the above results and discussion, we can reach the following conclusions:

(1) The sizes of the time-averaged cavity by both turbulence models are of qualitatively consistent trend compared to the experiment. The difference between LSM and FBM seems small.
(2) Overall, without cavitation, the numerical results by both turbulence models agree well with the experimental data. With cavitation the lift coefficient is under-predicted and drag coefficient is over-predicted by both turbulence models, but the trends are reasonably captured in the sheet and cloud cavitation regimes.
(3) Both computations and experiment indicate that as the AoA increases, the cavity exhibits more pronounced recurrence of the size variation.
(4) The TEM cavitation model details seem not critical for steady flow computations; however, they exhibit substantial variations for time-dependent computations.

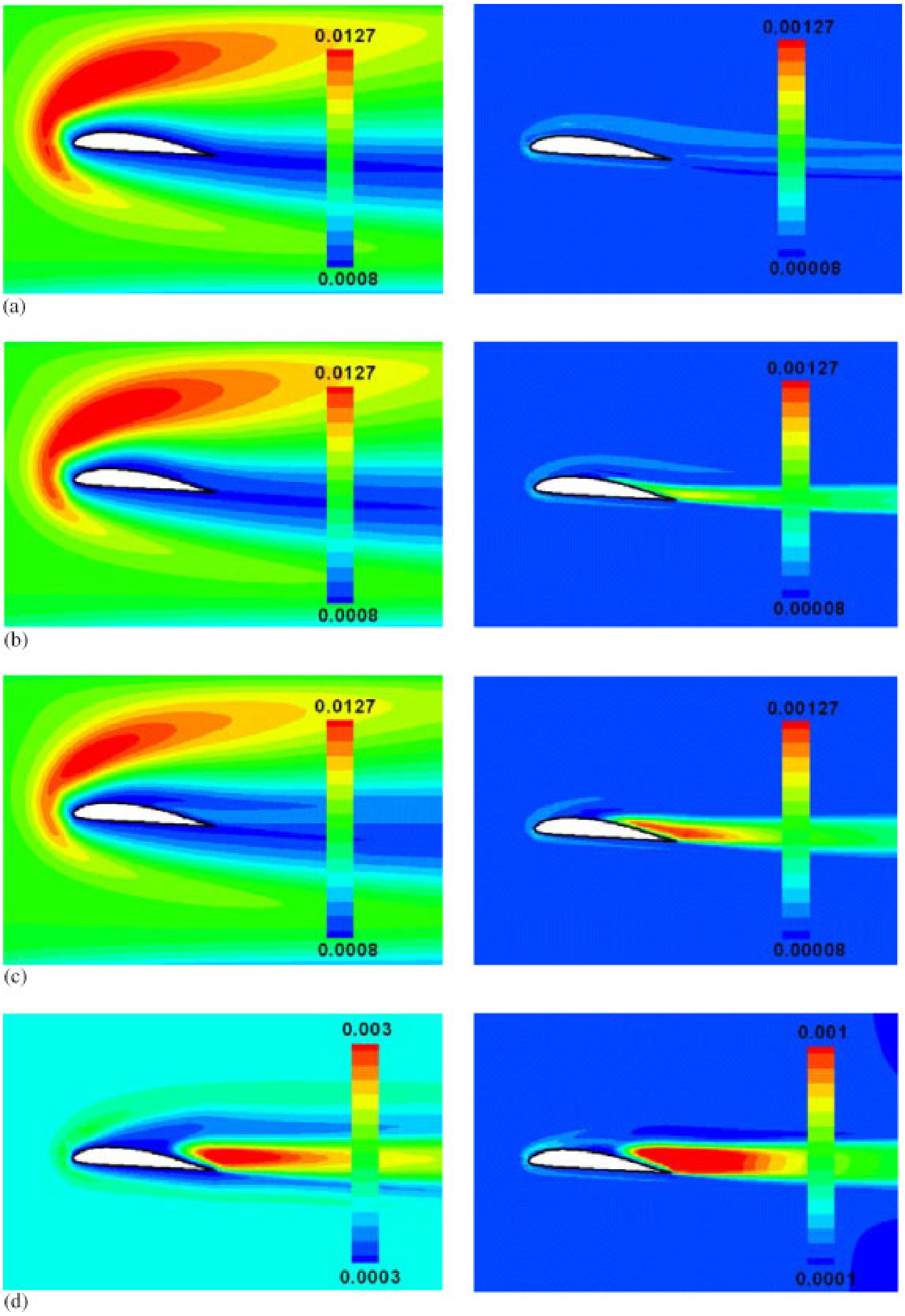

Figure 12. Time-averaged viscosity contours, AoA = 5°: (a) no-cavitation, $\sigma = 2.02$: LSM (left) and FBM (right); (b) inception, $\sigma = 1.12$: LSM (left) and FBM (right); (c) sheet cavitation, $\sigma = 0.92$: LSM (left) and FBM (right); and (d) cloud cavitation, $\sigma = 0.55$: LSM (left) and FBM (right).

(5) With both turbulence models, we observe that the eddy viscosity decreases as the cavitation becomes more pronounced and fluctuating in time. The LSM yields consistently higher eddy viscosity, resulting in reduced unsteadiness of the computed flow field. The FBM predicts stronger time dependency than the LSM due to reduced eddy viscosity levels.

In summary, the interplay between cavitation and turbulence models reveals that substantial differences in time-dependent flow results even though the time-averaged characteristics are similar. Such time-dependent effects have implication on impact on the solid structures.

ACKNOWLEDGEMENTS

The present effort has been supported by the NASA Constellation University Institute Program (CUIP), Ms Claudia Meyer program monitor. The study on cavitation phenomena at Dr Guoyu Wang's group is partly supported by the National Natural Science Foundation of China, project Number 50276004.

REFERENCES

1. Wang G, Senocak I, Shyy W, Ikohagi T, Cao S. Dynamics of attached turbulent cavitating flows. *Progress in Aerospace Sciences* 2001; **37**:551–581.
2. Singhal AK, Vaidya N, Leonard AD. Multi-dimensional simulation of cavitating flows using a PDF model for phase change. *ASME Fluids Engineering Division Summer Meeting*, *ASME Paper FEDSM1997-3272*, 1997.
3. Merkle CL, Feng J, Buelow PEO. Computational modelling of the dynamics of sheet cavitation. *3rd International Symposium on Cavitation*, Grenoble, France, 1998.
4. Kunz RF, Boger DA, Stinebring DR, Chyczewski TS, Lindau JW, Gibeling HJ, Venkateswaran S, Govindan TR. A preconditioned Navier–Stokes method for two-phase flows with application to cavitation prediction. *Computers and Fluids* 2000; **29**:849–875.
5. Ahuja V, Hosangadi A, Arunajatesan S. Simulations of cavitating flows using hybrid unstructured meshes. *Journal of Fluids Engineering* (ASME) 2001; **123**:331–340.
6. Venkateswaran S, Lindau JW, Kunz RF, Merkle CL. Computation of multiphase mixture flows with compressibility effects. *Journal of Computational Physics* 2002; **180**(1):54–77.
7. Senocak I, Shyy W. A pressure-based method for turbulent cavitating flow simulations. *Journal of Computational Physics* 2002; **176**(2):363–383.
8. Senocak I, Shyy W. Evaluation of cavitation models for Navier–Stokes computations. *2002 ASME Fluids Engineering Division Summer Meeting*, *ASME Paper FEDSM2002-31011*, 2002.
9. Senocak I, Shyy W. Computations of unsteady cavitation with a pressure-based method. *4th ASME-JSME Joint Fluids Engineering Conference*, *ASME Paper FEDSM2003-45009*, 2003.
10. Senocak I, Shyy W. Interfacial dynamics-based modelling of turbulent cavitating flows, part-1: model development and steady-state computations. *International Journal for Numerical Methods in Fluids* 2004; **44**:975–995.
11. Senocak I, Shyy W. Interfacial dynamics-based modelling of turbulent cavitating flows, part-2: time-dependent computations. *International Journal for Numerical Methods in Fluids* 2004; **44**:997–1016.
12. Wu J, Utturkar Y, Shyy W. Assessment of modelling strategies for cavitating flow around a hydrofoil. *5th International Symposium on Cavitation*, Osaka, Japan, Cav03-OS-1-12, 2003.
13. Vaidyanathan R, Senocak I, Wu J, Shyy W. Sensitivity evaluation of a transport-based turbulent cavitation model. *Journal of Fluids Engineering* 2003; **125**:447–458.
14. Wu J, Senocak I, Wang G, Wu Y, Shyy W. Three-dimensional simulation of turbulent cavitating flows in a hollow-jet valve. *Journal of Computer Modeling in Engineering and Sciences* 2003; **4**(6):679–689.
15. Wu J, Utturkar Y, Senocak I, Shyy W, Arakere N. Impact of turbulence and compressibility modelling on three-dimensional cavitating flow computations. *33rd AIAA Fluid Dynamics Conference and Exhibit*, *AIAA 2003-4264*, 2003.
16. Wu J, Johansen ST, Shyy W. Filter-based unsteady RANS computations for single-phase and cavitating flows. *ASME Heat Transfer/Fluids Engineering Summer Conference*, *ASME Paper HT-FED2004-56181*, 2004.
17. Coutier-Delgosha O, Fortes-Patella R, Rebound JL. Evaluation of the turbulence model influence on the numerical simulations of unsteady cavitation. *Journal of Fluids Engineering* 2003; **125**:33–45.
18. Launder BE, Spalding DB. The numerical computation of turbulent flows. *Computer Methods in Applied Mechanics and Engineering* 1974; **3**:269–289.

19. Smagorinsky J. General circulation experiments with the primitive equations I: the basic experiment. *Monthly Weather Review* 1963; 91–99.
20. Piomelli U. Large-eddy simulation: achievements and challenges. *Progress in Aerospace Sciences* 1999; **35**(4):335–362.
21. Moin P. Advances in large eddy simulation methodology for complex flows. *International Journal of Heat and Fluid Flow* 2002; **23**:710–720.
22. Sagaut P. *Large Eddy Simulation for Incompressible Flows*. Springer: Berlin, Germany, 2003.
23. Sandham ND, Alam M, Morin S. Embedded direct numerical simulation for aeronautical CFD. *Aeronautical Journal* 2001; **105**:193–198.
24. Mavridis C, Bakrozis A, Koutmos P, Papailiou D. Isothermal and non-premixed turbulent reacting wake flows past a two-dimensional square cylinder. *Experimental Thermal and Fluid Science* 1998; **17**:90–99.
25. Batten P, Goldberg U, Chakravarthy S. LNS—an approach towards embedded LES. *40th Aerospace Sciences Meeting and Exhibit*, *AIAA-2002-0427*, 2002.
26. Nichols RH, Nelson CC. Applications of hybrid RANS/LES turbulence models. *41st Aerospace Sciences Meeting and Exhibit*, *AIAA-2003-0083*, 2003.
27. Nakayama A, Vengadesan SN. On the influence of numerical schemes and subgrid-stress models on large eddy simulation of turbulent flow past a square cylinder. *International Journal for Numerical Methods in Fluids* 2002; **38**:227–253.
28. Breuer M, Jovicic N, Mazaev K. Comparison of DES, RANS and LES for the separated flow around a flat plate at high incidence. *International Journal for Numerical Methods in Fluids* 2003; **41**:357–388.
29. Johansen ST, Wu J, Shyy W. Filter-based unsteady RANS computations. *International Journal of Heat and Fluid Flow* 2004; **25**(1):10–21.
30. Kunz RF, Lindau JW, Kaday TA, Peltier LJ. Unsteady RANS and detached eddy simulations of cavitating flow over a hydrofoil. *5th International Symposium on Cavitation*, Osaka, Japan, Cav03-OS-1-12, 2003.
31. Shyy W, Wu J, Utturkar Y, Tai C-F. Interfacial dynamics-based model and multiphase flow computation. *Proceedings of the ECCOMAS 2004 Congress*, Jyväskylä, Finland, 2004.
32. Shyy W, Thakur S, Ouyang H, Liu J, Blosch E. *Computational Techniques for Complex Transport Phenomena*. Cambridge University Press: New York, 1997.
33. Shyy W. *Computational Modeling for Fluid Flow and Interfacial Transport*. Elsevier: Amsterdam, The Netherlands, 1997 (revised print).
34. Thakur S, Wright J, Shyy W. STREAM: a computational fluid dynamics and heat transfer Navier–Stokes solver theory and applications. *Technical Report*, Streamline Numerics Inc. and Computational Thermo-Fluids Laboratory, Department of Mechanical and Aerospace Engineering, Gainesville, FL, 2002.